

# The spatial organization of the chronnectome associates with cortical hierarchy and transcriptional profiles in the human brain

Jin Liu<sup>a,b,c,1</sup>, Mingrui Xia<sup>a,b,c,1</sup>, Xindi Wang<sup>a,b,c</sup>, Xuhong Liao<sup>a,b,d</sup>, Yong He<sup>a,b,c,\*</sup>

<sup>a</sup> State Key Laboratory of Cognitive Neuroscience and Learning, Beijing Normal University, Beijing 100875, China

<sup>b</sup> Beijing Key Laboratory of Brain Imaging and Connectomics, Beijing Normal University, Beijing 100875, China

<sup>c</sup> IDG/McGovern Institute for Brain Research, Beijing Normal University, Beijing 100875, China

<sup>d</sup> School of Systems Science, Beijing Normal University, Beijing 100875, China

## ARTICLE INFO

### Keywords:

Functional connectivity

Resting state fMRI

Gene expression

Gradient

Connectomics

Network dynamics

## ABSTRACT

The chronnectome of the human brain represents dynamic connectivity patterns of brain networks among interacting regions, but its organization principle and related transcriptional signatures remain unclear. Using task-free fMRI data from the Human Connectome Project (681 participants) and microarray-based gene expression data from the Allen Institute for Brain Science (1791 brain tissue samples from six donors), we conduct a transcriptome-chronnectome association study to investigate the spatial configurations of dynamic brain networks and their linkages with transcriptional profiles. We first classify the dynamic brain networks into four categories of nodes according to their time-varying characteristics in global connectivity and modular switching: the primary sensorimotor regions with large global variations, the paralimbic/limbic regions with frequent modular switching, the frontoparietal cortex with both high global and modular dynamics, and the sensorimotor association cortex with limited dynamics. Such a spatial layout reflects the cortical functional hierarchy, microarchitecture, and primary connectivity gradient spanning from primary to transmodal areas, and the cognitive spectrum from perception to abstract processing. Importantly, the partial least squares regression analysis reveals that the transcriptional profiles could explain 28% of the variation in this spatial layout of network dynamics. The top-related genes in the transcriptional profiles are enriched for potassium ion channel complex and activity and mitochondrial part of the cellular component. These findings highlight the hierarchically spatial arrangement of dynamic brain networks and their coupling with the variation in transcriptional signatures, which provides indispensable implications for the organizational principle and cellular and molecular functions of spontaneous network dynamics.

## 1. Introduction

The human brain is a highly dynamic and complex system that exhibits spontaneous fluctuations in neural activity over time. The emerging chronnectomics framework (Calhoun et al., 2014; Hutchison et al., 2013) describes the time-varying features of the functional covariation pattern among regions of the brain. Functional neuroimaging techniques (e.g., resting-state functional magnetic resonance imaging, rfMRI) (Biswal et al., 1995) have demonstrated certain nonrandom characteristics of dynamic brain networks at a macroscale, such as time-varying connectivity strength (Allen et al., 2014; Kang et al., 2011; Liao et al., 2015; Zalesky et al., 2014), modular reconfigurations (Liao et al., 2017) and individual uniqueness (Liu et al., 2018), as well as cyclical network transitions between states (Allen et al., 2014; Vidaurre et al., 2017; Zalesky et al., 2014). Importantly, these findings

imply a nonnegligible regional heterogeneity in the human chronnectome (Allen et al., 2014; Kang et al., 2011; Liao et al., 2017; Liao et al., 2015; Liu et al., 2018; Zalesky et al., 2014), with different brain regions playing distinct roles in the dynamic integration in the functional network. The spatial ordering of these regions in macroscopic network dynamics is still an underappreciated issue, although it is critical for providing insights into our understanding of the dynamic organization of functional network topologies.

The cortical functional hierarchy spanning from the primary sensorimotor cortex to transmodal areas is a fundamental organizational principle of the human brain (Huntenburg et al., 2018; Mesulam, 1998), which is also reported in the brains of nonhuman primates and even mice (Burt et al., 2018; Fulcher et al., 2019). Such a general principle has been observed both in microstructural characteristics, such as intracortical myelin content (Burt et al., 2018; Glasser and Van Essen, 2011)

\* Corresponding author at: State Key Laboratory of Cognitive Neuroscience and Learning, Beijing Normal University, Beijing 100875, China.  
E-mail address: [yong.he@bnu.edu.cn](mailto:yong.he@bnu.edu.cn) (Y. He).

<sup>1</sup> These authors contributed equally to this work

and the development sequence of subcortical white matter myelination (Fuster, 1997), and in macroscopic properties, such as functional connectivity features (Margulies et al., 2016) and the cycling transitions of metastates (Vidaurre et al., 2017) of brain functions. From an information processing perspective, the functional hierarchical organization of the brain allows efficient encoding and increased integration of information from sensation to cognition (Burt et al., 2018; Fulcher et al., 2019; Huntenburg et al., 2018; Mesulam, 1998). However, whether the spatial layout of intrinsic dynamic networks of the human brain follows the principle of cortical functional hierarchical ordering remains unknown.

If the spatial configurations of brain network dynamics reflect the general cortical functional hierarchy, we speculate that a molecular program might exist for coding this layout of the human connectome across the cortex. Recently, the integration of postmortem gene expression with *in vivo* neuroimaging data has provided unprecedented opportunities for bridging the gap between macroscopic network properties and the transcriptional signatures of the brain (Fornito et al., 2019; Hawrylycz et al., 2012; Richiardi et al., 2015). For example, several previous studies observed that the modular and hub architectures of static functional networks during rest are associated with gene expression involving ion channel activity (Richiardi et al., 2015) and oxidative metabolism/mitochondria (Vertes et al., 2016), respectively. During task states, the convergence of dynamic streams of functional networks is linked with the expression of synaptic long-term potentiation genes (Diez and Sepulcre, 2018). Notably, these previous studies mainly focused on static functional networks or the task state dynamics and did not provide direct evidence of the transcriptional profiles related to the intrinsic functional network dynamics that reflect the temporal organization of spontaneous fluctuations of neural activity in the resting human brain (Calhoun et al., 2014; Deco et al., 2013). Clarifying this issue will not only provide insight into the transcriptional correlates of intrinsic network dynamics but also have indispensable implications for the understanding and interpretation of chronnectomics in normal development, aging, and disorders.

To address these issues, we conducted a transcriptome-chronnectome association study to investigate the spatial configurations and related transcriptional profiles of brain network dynamics by employing rfMRI data from the Human Connectome Project (HCP; 681 participants) (Van Essen et al., 2013) and microarray-based gene expression data from the Allen Institute for Brain Science (AIBS; 1791 samples from the brains of six donors) (Hawrylycz et al., 2012). We defined four categories of dynamic brain nodes in terms of their time-varying patterns in global connectivity variations and modular switching (See *Methods and materials*). Specifically, we used temporal global variability (tGV) to measure the overall fluctuations of a brain node in connectivity with all of the other nodes within the network over time (Allen et al., 2014; Choe et al., 2017; Elton and Gao, 2015; Fong et al., 2019; Kruschwitz et al., 2015; Liu et al., 2018). However, nodes with the same value of tGV may interact frequently with a set of very local nodes around them or with a set of distributed nodes that belong to different modules in the brain network, which could lead to distinct roles in contribution to the dynamic integration. Thus, we further used temporal modular variability (tMV) to measure time-varying extents of a brain node in switching among different modules (Bassett et al., 2011; Braun et al., 2015; Liao et al., 2017; Shine et al., 2016; Telesford et al., 2016). As a result, we combined tGV and tMV together to characterize the roles of network nodes in dynamic integration by considering both global and modular temporal variability. Then, we compared the spatial organization of four categories of dynamic brain nodes with cortical functional hierarchy (Mesulam, 1998), T1w/T2w (Glasser et al., 2016; Glasser and Van Essen, 2011), primary connectivity gradient maps (Margulies et al., 2016), and cognitive term maps (Poldrack et al., 2012) ([www.neurosynth.org](http://www.neurosynth.org)). Finally, we established the associations between the expression profiles of genes and the spatial pattern of network dynamics across regions.

## 2. Methods and materials

### 2.1. HCP datasets

The resting-state fMRI (rfMRI) data of 832 participants with four complete scanning runs were initially obtained from the publicly available S900 Data Release of the Human Connectome Project (HCP) (Van Essen et al., 2013). Participants with arachnoid cysts were excluded according to visual inspection of their T1-weighted images ( $n = 25$ ). Then, data from twelve participants were excluded because of missing time points in the rfMRI data in any of the four runs. Data from one hundred and fourteen participants with excessive head motion (above 3 mm or 3° in any direction) in any of the four runs were further excluded. Finally, data from the remaining 681 participants (age:  $28.7 \pm 3.7$  years, range: 22–37 years, 381 females) were used for the following analyses.

Multiband gradient-echo-planar whole-brain imaging acquisitions were acquired on a 3T Siemens Connectome Skyra scanner at Washington University, USA. The rfMRI data were obtained with the following sequence parameters: repetition time (TR) = 720 ms, echo time (TE) = 33.1 ms, flip angle (FA) = 52°, bandwidth = 2290 Hz/pixel, field of view (FOV) =  $208 \times 180$  mm<sup>2</sup>, matrix =  $104 \times 90$ , 72 slices, voxel size =  $2 \times 2 \times 2$  mm<sup>3</sup>, multiband acceleration factor = 8, and 1200 volumes (14 min and 24 s) for each run. For each participant, four rfMRI runs were acquired in two days, where one session containing two rfMRI runs was performed each day. During the scan, participants were instructed to keep their eyes open with fixation. After the HCP minimal preprocessing procedure (Glasser et al., 2013), we further used SPM12 ([www.fil.ion.ucl.ac.uk/spm/](http://www.fil.ion.ucl.ac.uk/spm/)) and GREYNA (Wang et al., 2015) to reduce the biophysical noise in the rfMRI data by regressing out the linear trend, 24 head motion parameters, cerebrospinal fluid, white matter, and global signals and performing temporal bandpass filtering (0.01–0.1 Hz).

### 2.2. AIBS datasets

The microarray-based gene expression data in human brain tissue were downloaded from the AIBS website (January 2018) (Hawrylycz et al., 2012). The tissue samples were collected from six brains of adult donors, two of which were complete brains, while the remaining four samples were left hemispheres (Table S1). The acquisition methods and processing procedures of these samples are described in a technical paper ([http://help.brain-map.org/display/humanbrain/Documentation?preview=/2818165/8454282/WholeBrainMicroarray\\_WhitePaper.pdf](http://help.brain-map.org/display/humanbrain/Documentation?preview=/2818165/8454282/WholeBrainMicroarray_WhitePaper.pdf)). Briefly, each hemisphere of the brain was first dissected into approximately 500 anatomically discrete samples. The precise number of samples for each donor is presented in Table S1. Then, each sample was spatially registered to the Montreal Neurological Institute (MNI) coordinate space according to the T1-weighted image obtained before dissection, and the locations of all samples are given in MNI coordinates in *SampleAnnot.csv* of each donor's microarray data files. Normalization processes were conducted to minimize the potential effects of nonbiological biases and to ensure the gene expression data were comparable among samples within and across the brains. The detailed normalization methods are described in a technical paper for microarray data normalization ([http://help.brain-map.org/display/humanbrain/Documentation?preview=/2818165/5177355/Normalization\\_WhitePaper.pdf](http://help.brain-map.org/display/humanbrain/Documentation?preview=/2818165/5177355/Normalization_WhitePaper.pdf)). The normalized gene expression data of 58,692 probes were available for each sample.

### 2.3. Constructing dynamic brain networks

For each participant, whole-brain dynamic functional networks were constructed based on the preprocessed rfMRI data in each run. Here, a multimodal brain atlas (Glasser et al., 2016) was employed to parcellate the cerebral cortex into 360 regions as network nodes.

Specifically, a volume-based Glasser-360 atlas was generated using the HCP workbench ([www.humanconnectome.org/software/connectome-workbench](http://www.humanconnectome.org/software/connectome-workbench)). First, the surface-based Glasser-360 atlas (fs\_LR\_32k surface) and the averaged T1w volume template from the 210P dataset (<https://balsa.wustl.edu/WN56>) (Glasser et al., 2016) were obtained. The mid-thickness surface template of the surface-based Glasser-360 atlas was used to determine the coordinates of the voxel extracted from the T1w volume template, and the inner and outer surface templates of the surface-based Glasser-360 atlas were used to constrain the boundaries of the extraction algorithm. Label-to-volume mapping in the HCP workbench was then performed using the ribbon-constrained mapping algorithm to generate the volume-based Glasser-360 atlas. The time series for each node was extracted by averaging the time courses of all voxels within the region. The dynamic functional networks were then constructed using a commonly used sliding window approach. Notably, the time window had a width of 100 s (i.e., 139 TRs), which was shifted in time with a step of 0.72 s (i.e., 1 TR), allowing sufficient time points to estimate dynamic functional connectivity at the low-frequency band of interest (0.01–0.1 Hz) and to simultaneously capture temporal variations during a short period (Liao et al., 2017, 2015; Liu et al., 2018; Telesford et al., 2016). Within each window, we estimated the functional connectivity matrix by calculating the Pearson's correlation between any pair of network nodes based on the segments of the time series in the window. Therefore, for each of the four runs, for each participant we obtained individual dynamic brain networks with 1062 360 × 360 connectivity matrices (i.e., windows).

#### 2.4. Aligning AIBS datasets to brain atlas

To match the gene expression data from AIBS and the brain parcellation used in dynamic network construction, we performed several pre-processes for the gene expression microarray data of the brain samples, including mapping samples to network nodes, probe reannotation and selection, and normalization across donors. Briefly, a total of 1791 brain tissue samples from six donors were first referenced to the 360-region brain parcellation according to their MNI coordinates (Krienen et al., 2016; Richiardi et al., 2015; Whitaker et al., 2016). Specifically, if a sample did not fall within any region, we extended the matching range to a radius of 5 mm to search for the nearest brain region. The final distribution of the samples covered 84% of the parcellation (i.e., 301/360). Notably, the assigned samples were distributed evenly among the four categories of dynamic network nodes. Subsequently, we used the Reannotator toolkit (Arloth et al., 2015) to reannotate the gene assignment of probes with the reference genome assembly hg19 (Kent et al., 2002) and excluded probes that were not assigned to any gene and those with more than two mismatches between their sequences and reference. We also removed the probes without an Entrez ID or with significant calls in fewer than 50% of the assigned samples across all donors (the Entrez ID and call information of all probes are available from AIBS; please find the Probes.csv and PACall.csv files in the data folder of each donor). These procedures resulted in 32,191 probes corresponding to 16,392 genes. Then, for each gene in each donor, we averaged the expression level across probes in each sample, followed by Z-score normalization (subtracting the mean and dividing by the standard deviation) across the samples and further averaging of the Z-scores of all samples within a network node. Finally, a gene expression map at the group level was obtained by averaging the Z-scores of the gene expression level across the six donors. Notably, the preprocessing procedures here are very similar to the seven-step analysis pipeline proposed by Arnatkeviciute et al. (2019), except for the last two steps, namely, gene filtering and accounting for spatial effects. These two steps were related to the hypothesis or research question in the study. Here, studying the transcriptional profile related to the spatial layout of dynamic networks, we sought to explore the whole-brain genome-wide gene expression pattern over any specific gene set. Considering spatial effects, we employed spin tests (spatial permutation test con-

sidering spatial autocorrelation) (Alexander-Bloch et al., 2018) (<https://github.com/jinliu-bnu/Liu-et-al.-2019/tree/master/SpinTest>) to reduce the potential influence on our findings.

#### 2.5. Estimating dynamic characteristics of brain networks

As described previously, for each participant we obtained individual dynamic brain networks with 1062 360 × 360 connectivity matrices (each of four scanning runs). For each network node, we computed two dynamic measures: tGV, which represents the overall fluctuation amplitude of the node's connections (Liu et al., 2018), and tMV, which represents the degree of variation in module affiliations across time (Liao et al., 2017). The procedures in details can be found in our previous studies (Liao et al., 2017; Liu et al., 2018) and were briefly described here.

i) tGV. For functional connectivity between node  $i$  and node  $j$ , we first calculated its temporal variability,  $tV_{(i,j)}$ , as follows:

$$tV_{(i,j)} = \frac{1}{F} \sum_{F_f=1}^F A_{f(i,j)} \quad (1)$$

where  $A_{f(i,j)}$  is the fluctuation amplitude of the functional connectivity (Allen et al., 2014; Liu et al., 2018) across windows between node  $i$  and node  $j$  at a given frequency range  $f$ , and  $F$  is the number of discrete low frequencies of interest. The low-frequency threshold was set at 0.08 Hz, corresponding to 80% of the energy of the frequency spectrum (Liu et al., 2018). Then, for a given node, we calculated its tGV by summing the temporal variability of all the functional connections linking to this node, as follows:

$$tGV_i = \sum_{j=1, i \neq j}^N tV_{(i,j)} \quad (2)$$

where  $tV_{(i,j)}$  is the temporal global variability in functional connectivity between node  $i$  and node  $j$ , ( $j = 1, 2, 3, \dots, N, i \neq j$ ), and  $N$  is the total number of nodes (i.e., 360). Notably, tGV <sub>$i$</sub>  represents the overall fluctuations of connectivity for a given node  $i$  over time. Nodes with high tGV tend to have great temporal changes in the network wiring profile at the global level.

ii) tMV. For each individual, we first detected the modular architectures of the dynamic functional networks by applying the InfoMap algorithm (Power et al., 2011; Rosvall and Bergstrom, 2008) to the thresholded functional connectivity matrices. The network density was set to 15% as in our previous work (Liao et al., 2017), which can maintain the connectedness of the dynamic networks for most participants. The module detection processes were repeated 100 times for each matrix/time window, and the modular architecture with the shortest description length (precluding situations in which there was only one module for the network) was chosen as the final module partition. Briefly, we first selected the modular partition of the window with the highest adjusted mutual information (Vinh et al., 2010) with all the other windows for each participant. Then, the modular partitions were aligned across all participants. The typical modular partition was finally obtained by assigning each node with its most frequently labeled module among participants. Then, for each node, the modular variability,  $MV_i(k, l)$ , between two modular affiliations (Steen et al., 2011) of different time windows in the dynamic networks was calculated as follows:

$$MV_i(k, l) = 1 - \frac{|M_i(k) \cap M_i(l)|}{|M_i(k)|} \cdot \frac{|M_i(k) \cap M_i(l)|}{|M_i(l)|} \quad (3)$$

where  $MV_i(k, l)$  denotes the modular variability for a given region  $i$  between time window  $k$  and  $l$  ( $k = 1, 2, 3, \dots, T; l = 1, 2, 3, \dots, T; k \neq l$ );  $T$  is the number of time windows;  $M_i(k)$  and  $M_i(l)$  are the module affiliation of node  $i$  in time window  $k$  and  $l$ , respectively;  $M_i(k) \cap M_i(l)$  represents the shared node set between modules  $M_i(k)$  and  $M_i(l)$ , and  $|M_i(k) \cap M_i(l)|$  is the number of nodes in the shared node set. For a given

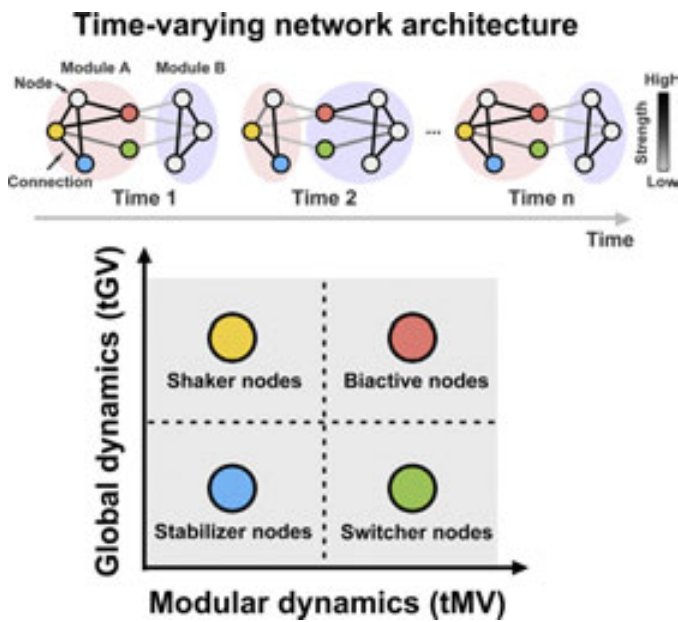


**Fig. 1.** Diagram of the different categories of network node dynamics. Different nodes have distinct patterns of temporal variations in global connectivity and modular affiliations across time. The strength of network connections from weak to strong is rendered from light gray to black. Each light circle represents a unique module composed of a set of nodes. The four categories of nodes are shown in different colors according to their dynamic metrics compared with the mean values of each measure: the shaker nodes exhibit large global fluctuations but limited modular dynamics (yellow); the biactive nodes have notable global and modular dynamics (red); the switcher nodes show frequent modular variations but less global dynamics (green); and the stabilizer nodes exhibit very little global and modular dynamics (blue).

node, the total modular variability across all the windows was further calculated as follows (Liao et al., 2017):

$$MV_i = \sum_{k=1}^T w_k MV_i(k) \quad (4)$$

where  $MV_i(k) = \sum_{k \neq l} MV_i(k, l) / (T - 1)$  denotes the average modular variability for node  $i$  between the modular partition of window  $k$  and that of all of the other windows, and  $w_k$  is a normalized weight coefficient considered in the formula to reduce the bias of potential outlier time windows, which is estimated using the adjusted mutual information. Notably, tMV represents the variation degree of modular switching among different modules for a given node over time. Nodes with high tMV participate more frequently in modular reorganization in dynamic networks than nodes with low tMV.

Finally, for each participant, the two dynamic maps (i.e., tGV and tMV) were obtained by averaging the dynamic maps between the two runs for each session.

### 2.6. Characterizing spatial patterns of brain network dynamics

The tGV and tMV maps were jointly used to characterize the spatial organization of dynamic brain networks. As shown in the example diagram (Fig. 1), in the current study we combined tGV and tMV together to classify network nodes into four distinct categories: shaker nodes with large global variations but limited module switching ( $\uparrow$ tGV and  $\downarrow$ tMV, yellow), biactive nodes with high dynamics at both the global and modular levels ( $\uparrow$ tGV and  $\uparrow$ tMV, red), switcher nodes with frequent transitions between modules but lower global variations ( $\downarrow$ tGV and  $\uparrow$ tMV, green), and stabilizer nodes with relatively stable temporal variations ( $\downarrow$ tGV and  $\downarrow$ tMV, blue).

To obtain the group-level tGV and tMV maps, we first averaged each dynamic measurement across all participants within each session. Then, for each dynamic measurement, we assessed the reliability by calculating Pearson's correlation on the spatial pattern between the two sessions. Notably, both the tGV and tMV maps were almost identical between the two sessions (Fig. S1). Thus, we generated the final group-level tGV and tMV maps by averaging the session-averaged maps across all individuals. Based on these two group-based, session-averaged maps, as shown in Fig. 2a, we divided the network nodes into four categories, according to the comparisons with each mean measurement across all nodes. Additionally, as a supplementary analysis, we examined whether a node significantly belonged to a category across the participants. Briefly, we performed z-score transformation for tGV and tMV for each participant and explored whether the tGV/tMV was significantly higher or lower than zeros for each node across participants by using one-sample  $t$ -tests. Then, we divided the network nodes into four categories according to the statistical results compared with zeros (i.e., mean).

### 2.7. Association between brain network dynamics and cortical functional hierarchy/connectivity gradient/microstructural/cognitive term maps

To explore whether the spatial layout of brain network dynamics can reflect the general cortical hierarchy, we assigned each of the 360 regions to one of four cortical types in the cortical functional hierarchy as described by Mesulam (1998) (i.e., primary, unimodal association, heteromodal association, and paralimbic/limbic areas) (Fig. S1). Specifically, the cortical functional hierarchy assignment for each region followed these criteria: (i) The classical figure/map of cortical hierarchy and descriptions from Mesulam (1998) were taken as a fundamental reference in which the Brodmann areas (BAs) have been labeled over the whole-brain cortex and allocated among four types of hierarchy. This map has been widely adopted and cited in several cognitive neuroscience reviews (Ffytche and Wible, 2014; Kiehl, 2006). (ii) The BA labels for each of the 360-atlas nodes were extracted from Glasser et al. (2016). For nodes without a clear BA label, we overlaid them on the BA template provided in MRICroN and assigned each node with the BA label corresponding to the area that included the largest number (which should be more than half) of the voxels within the node. Then, the nodes were initially assigned to one of the four hierarchical types according to their BA labels. (iii) For nodes for which a BA label could not be obtained, we inspected their anatomical locations and their adjacent landmark gyrus or sulcus, compared them with the cortical hierarchy figure, and assigned the node to one of the four hierarchical types. (iv) Notably, some BAs were distributed in two or more functional hierarchies. In these cases, we further examined the anatomical location and boundary of nodes involving these BAs and finely corrected their hierarchy types according to their adjacent landmark gyrus or sulcus in the classical figure (Mesulam, 1998, 2000). All visual inspections were performed by two experienced cognitive neuroscience researchers. The final cortical hierarchy assignments for Glasser's 360-atlas are available at <https://github.com/jinliu-bnu/Liu-et-al.-2019>.

Within each type of hierarchical area, we calculated the overlapping percentiles of the four categories of the dynamic network nodes. The spin test (Alexander-Bloch et al., 2018) (<https://github.com/jinliu-bnu/Liu-et-al.-2019/tree/master/SpinTest>), a spatial permutation framework considering the spatial autocorrelation, was used to determine whether each proportion was significantly larger than that by chance. Briefly, given that the spin spatial permutation is a surface-based framework, we first mapped the spatial distribution of dynamic network node types onto the cortical surface, and a node type assignment was obtained for each vertex. In each permutation, dynamic network node types on spherical representations of the cortical surface were randomly rotated. For a given node, the surrogated type was assigned as the type with the greatest number of vertices within this node. The permutation was repeated 10,000 times, and thus, a null model was obtained for the spatial distribution of the four node types. Then, the real overlapping per-

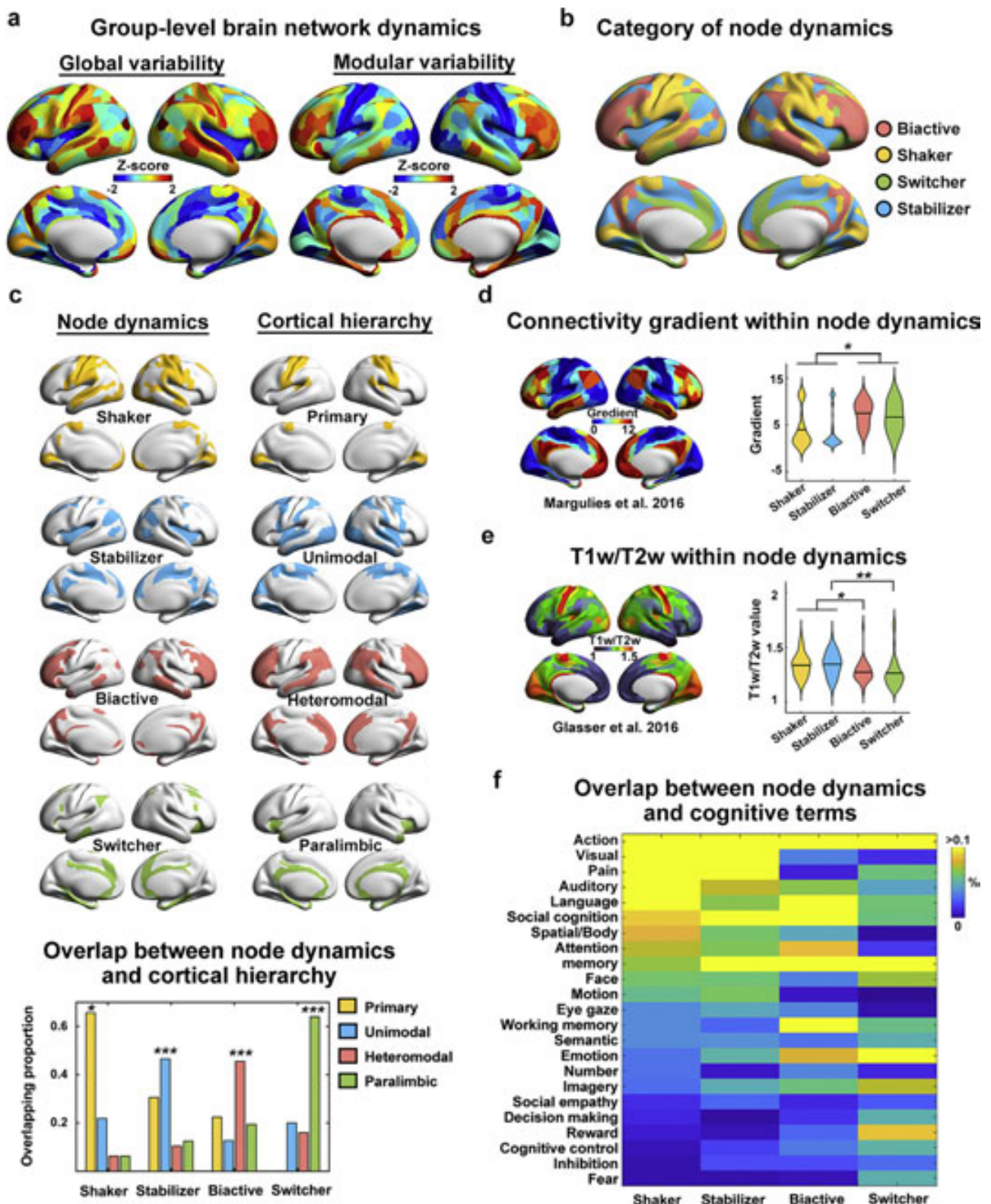


Fig. 2. Spatial layout and microstructural relevance of the four categories of nodes in dynamic brain networks. a) The group-level maps of global and modular dynamics were obtained by averaging the individual brain activity maps. b) The spatial distribution of the four categories of nodes in the dynamic brain networks. c) The spatial distribution of each category of the dynamic network nodes and of each type of cortical hierarchy area (top). The overlapping proportions of the four categories of network nodes in each type of cortical hierarchy area. Spin tests were conducted to determine whether the proportions were significantly higher than chance (bottom). d) Between-group differences in the primary gradient (left, Margulies et al., 2016) across four categories of dynamic nodes. The biactive nodes and the switcher nodes had a significantly higher gradient than the shaker nodes and the stabilizer nodes (right, spin tests). e) Between-group differences in T1w/T2w (left, Glasser et al., 2016) across the four categories of dynamic nodes. The transmodal nodes exhibited significantly lower T1w/T2w values than the stabilizer nodes, and the shaker nodes exhibited significantly higher T1w/T2w values than the biactive nodes and the switcher nodes at a marginally significant level (right, spin tests). f) The overlapping proportion of four categories of network nodes with each cognitive term map available from topic-based meta-analyses (Poldrack et al., 2012) based on the NeuroSynth metanalytic database. The surface rendering was generated using BrainNet Viewer ([www.nitrc.org/projects/bnv/](http://www.nitrc.org/projects/bnv/)) (Xia et al., 2013) with the inflated cortical 32K surface (Glasser et al., 2016). \* $p < 0.05$ ; \*\* $p < 0.01$ ; \*\*\* $p < 0.001$ .

centiles of each category of dynamic nodes on each hierarchical area were examined based on this null model.

The primary gradient of connectivity has been found to show a cortical hierarchy span from the sensorimotor cortex to the association cortex (Margulies et al., 2016). Here, we compared the distribution of four types of dynamic nodes with the primary connectivity gradient map reported by Margulies et al. (2016) by comparing the average gradient value among four types of dynamic nodes. Moreover, the ratio of T1- and T2-weighted MRI (Glasser et al., 2016; Glasser and Van Essen, 2011) has been found to be sensitive to the intracortical myelin content and many other microstructural properties involving cell size and density, and it has been considered a reliable noninvasive neuroimaging measure for indexing cortical hierarchy (Burt et al., 2018). Here, we compared the T1w/T2w ratio values among the four categories of dynamic nodes by employing a group-averaged, publicly available T1w/T2w map (Glasser et al., 2016; Glasser and Van Essen, 2011). Spin tests were performed to determine whether the mean gradient value or T1w/T2w was significantly different between each pair of dynamic network node categories (10,000 times). Finally, we sought to establish an association between four types of dynamic nodes and the cognitive term maps available from topic-based meta-analyses (Poldrack et al., 2012) based on the NeuroSynth metanalytic database ([www.neurosynth.org](http://www.neurosynth.org)). Specifically, we calculated the ratio of the number of overlapping voxels divided by the number of total voxels between each type of dynamic nodes and each cognitive term map. To match the cognitive term maps from NeuroSynth, we first extended the boundaries of mid-thickness of the surface-based Glasser-360 atlas with 6 mm and generated the volume-based atlas mask for each type of dynamic node. Then, we matched each mask with the set of 50 topic terms in NeuroSynth ([www.neurosynth.org/analyses/topics/v5-topics-50/](http://www.neurosynth.org/analyses/topics/v5-topics-50/)). Among 50 maps, we removed 27 terms due to nonoverlapping or because they did not reflect any cognitive function. The 23 topic terms remained for the analyses.

### 2.8. Association between brain network dynamics and transcriptional signatures

To explore the transcriptional profile that could explain the spatial variation in intrinsic functional dynamic properties of the resting human brain, we used partial least squares regression (PLSR), which is applicable when the observations (i.e., 301 nodes/regions) are fewer than the predictor variables (i.e., 16,392 genes), and it has been used in several previous studies (Seidlitz et al., 2018; Vertes et al., 2016; Whitaker et al., 2016). The PLSR analysis can define several components, each of which is the linear combination of the gene expression of predictor variables that can explain most of the variance of dynamic measurements in response variables. Briefly, the predictor variables matrix  $X$  and the response variables matrix  $Y$  are first centered, resulting in  $X_0$  and  $Y_0$ , respectively. The component  $i$  of the PLSR is then weighted by  $p_i$  and  $q_i$  to calculate the component scores  $T_i$  and  $U_i$  for  $X_0$  and  $Y_0$ , respectively:

$$T_i = X_0 p_i + E \tag{6}$$

$$U_i = Y_0 q_i + F \tag{7}$$

where  $E$  and  $F$  are the error terms. Then, the weight vector  $p_i$  and  $q_i$  and the component scores  $T_i$  and  $U_i$  are estimated to ensure the maximum covariance between  $T_i$  and  $U_i$ . Thus, the regression of predictor variables and response variables can be defined as follows:

$$U_i \sim T_i \tag{8}$$

or

$$Y_0 q_i = B_{0i} + B_{1i} X_0 p_i + G \tag{9}$$

where  $G$  is the error term, and  $B_{1i}$  and  $B_{0i}$  are the regression coefficient and intercept, respectively. The  $R^2$  of the fitting for each component is used to illustrate how much the predictive variables can explain the variance of the response variables. Here, in our PLSR model, the gene expression data of brain nodes (301 nodes  $\times$  16,392 genes) were set as the predictor variables  $X$ , and the values of tGV and tMV of brain nodes (301 nodes  $\times$  2 measures) were set as the response variables  $Y$ . The PLSR analysis was performed by employing the code shared by Whitaker et al. (2016), which uses a SIMPLS algorithm. Notably, the SIMPLS algorithm provides an alternative approach for PLSR that is fast and easier to interpret. The components are calculated directly as linear combinations of the original centered data, which avoids deflating the data by weights during the calculation of new components. Thus, the number of components chosen for the PLSR model did not influence every single component. Here, we initially set the number of components to 10 in the PLSR to explore the component composition. The output of components from PLSR was ranked by covariance between predictor variable  $X$  and response variable  $Y$ ; thus, the first few components could provide the optimal low-dimensional representation for the covariance between the two data sets (the gene expression and the dynamic characteristics) with higher dimensions. The statistical significance of the goodness of fit of the components from PLSR was determined using a spin test. Briefly, we mapped the spatial distribution of dynamic characteristic (i.e., tGV and tMV) onto the cortical surface, and tGV and tMV values were obtained for each vertex. In each permutation, dynamic values of the spherical representations of the cortical surface were randomly rotated. For a given node, the surrogated tGV and tMV values was assigned as the mean values of vertexes within this node. Then, the surrogated dynamic values were used as the response variable in PLSR and the  $R^2$  was recorded. The permutation was repeated 10,000 times to generate the null model based on the spin test. The real  $R^2$  of the first few components that explained over ten percentages of the variance in the response variables was compared with this null-model to determine whether the real  $R^2$  was significantly larger than that by chance. Then, for significant components, we used a bootstrapping method to assess the estimation error of the weight for each gene and further divided the weight by the estimated error to obtain the corrected weight for each gene (Whitaker et al., 2016). We ranked the genes according to their corrected weights, which represent their contribution to the PLSR component. The Gene Ontology enrichment analysis and visualization tool (GORilla, <http://cbl-gorilla.cs.technion.ac.il/>) (Eden et al., 2009) was used to identify the enriched Gene Ontology terms of the ranked genes from each significant component. Specifically, we used a  $p$ -value threshold of  $10^{-6}$  in the advanced parameters settings and applied the Benjamini–Hochberg false discovery rate (FDR) method to correct for the multiple tests. In the main results, the Gene Ontology terms with an FDR  $q$ -value below 0.01 were reported (Table S2). The Reduce Visualize Gene Ontology (REVIGO, <http://revigo.irb.hr/>) tool was used to summarize the obtained Gene Ontology terms by removing redundant terms. Furthermore, we calculated the average expression of the top-ranked related genes (top 10%) in each significant component for each category of dynamic nodes to delineate their different transcriptional features. Spin tests were performed to determine whether the gene expression was significantly different between each pair of dynamic network node categories (10,000 times).

### 2.8. Validation analyses

To assess the reliability of our results, we performed the following analyses.

- (i) *The effect of head motion.* We excluded participants with large head motion (above 3 mm or 3° in any direction and in any run) and regressed out 24 head motion parameters. To further strictly control the potential influence of head motion on our main findings, we performed spike regression-based scrubbing in the nuisance regression

procedure (Power et al., 2015; Yan et al., 2013) during preprocessing with the criterion of a framewise displacement above 0.5 mm and repeated our main analyses above.

- (ii) *The effect of dynamic network construction.* To validate the potential effect of the sliding window-based network construction approach on our main results, we employed the framewise dynamic conditional correlation (DCC) method (Lindquist et al., 2014) to reconstruct the dynamic networks and repeated our analysis. The DCC is a model-based approach defining dynamic correlations of time courses. Based on quasi-maximum likelihood methods, the DCC can effectively estimate all of the model parameters. The DCC algorithm mainly includes two steps. First, a univariate generalized autoregressive conditional heteroskedasticity model was fit to each time course and further used to estimate standardized residuals. Second, an exponential weighted moving average-type approach was applied to these standardized residuals to compute the time-varying correlation. For details, see Lindquist et al. (2014).
- (iii) *Effect of the individual differences on dynamic measures.* To further investigate the potential influence of individual differences on dynamic characteristics, we performed one-sample *t* tests of tGV and tMV for each node. The *t* maps are controlled for individual differences by considering variations across participants as compared to the mean maps. The main analyses were repeated in terms of these *t* maps.
- (iv) *Effect of the negative connectivity and network threshold on tMV calculation.* For the tMV estimation, we applied the infomap algorithm to detect modular structure in each connectivity matrix/window. This algorithm has been widely used and has revealed reliable modular structures across connectome studies (Liao et al., 2017; Power et al., 2010; Rubinov and Sporns, 2010). Notably, most of the previous studies applied thresholding operations on the raw correlation matrix to capture the core architecture of the brain network. Thus, we thresholded the raw correlation matrix to retain the top 15% connections (i.e., the negative correlations were naturally removed) for module detection in the main analyses. To explore the potential influence of negative connectivity and the network threshold, we re-performed the modular analysis without matrix thresholding and the negative correlations were included. Given that the infomap algorithm cannot handle negative values, we applied the Louvain community detection algorithm (Brain Connectivity Toolbox, [www.nitrc.org/projects/bct/](http://www.nitrc.org/projects/bct/)) for each matrix/window and estimated tMV map for each individual. A group-averaged tMV map was then calculated by averaging the tMV across runs and participants.
- (v) *The reproducibility of results using a half-split strategy.* Briefly, we split the rfMRI data of the HCP datasets into two cohorts matched for age, gender and handedness and obtained the group-level tGV and tMV maps within each subgroup (i.e., HCP-cohort1 and HCP-cohort2). For the gene expression data from the AIBS datasets, we split six brains into two subgroups as in a previous study (Richiardi et al., 2015), in which each subgroup included a full brain (H0351.2001 or H0351.2002) and two half-brains from the other donors to balance the sample size, resulting in six possible subgroup pairs (see Table S3). For each subgroup pair of AIBS datasets, we repeated the PLSR with two cohorts of HCP (i.e., 2 subgroups  $\times$  6 pairs  $\times$  2 cohorts = 24 repetitions). Then, we performed the enrichment analysis for each repetition and compared the results with those obtained in the main analysis.

### 3. Results

#### 3.1. The spatial pattern of the human chronnectome reflects cortical functional hierarchy

For each individual, we mapped the dynamic network activities in terms of the tGV and tMV maps. Both maps exhibited a high spatial sim-

ilarity between sessions (tGV:  $r = 0.99$ , tMV:  $r = 0.97$ , all  $p < 0.0001$ , Fig. S1). Based on two group-based, session-averaged tGV and tMV maps (Fig. 2a), the network nodes were further divided into four categories according to their temporal dynamics in global variations and modular switching (in comparisons with each mean measurement across all nodes). As shown in Fig. 2b, the shaker nodes ( $\uparrow$ tGV and  $\downarrow$ tMV) were primarily located in the sensorimotor cortex, including the primary visual, motor, somatosensory and auditory cortices; the biactive nodes ( $\uparrow$ tGV and  $\uparrow$ tMV) were primarily in the lateral and medial frontal and parietal cortices; the switcher nodes ( $\downarrow$ tGV and  $\uparrow$ tMV) were mainly in the anterior and middle cingulate cortices, the medial temporal lobe, and the anterior insula; and the stabilizer nodes ( $\downarrow$ tGV and  $\downarrow$ tMV) were mainly in the sensorimotor association cortices, the supplementary motor cortices, and the posterior insula. The findings of the four-category nodes were largely conserved when using a threshold of one standard deviation above mean (Fig. S1).

We found that the spatial layouts of the four categories of dynamic network nodes were generally similar to the cortical hierarchy distributions (Fig. 2c, top). Specifically, the brain regions within each hierarchical type were significantly dominated by a particular category of dynamic nodes (all  $p < 0.012$ , 10,000 permutations, spin tests; the same below): the primary area was mostly occupied by shaker nodes, the unimodal association area was largely occupied by stabilizer nodes, the heteromodal association area was primarily occupied by biactive nodes, and the paralimbic/limbic area was mainly dominated by switcher nodes (Fig. 2c, bottom). Then, we compared the distribution of dynamic nodes and the principal gradient reported by Margulies et al. (2016) and found that the transmodal nodes (i.e., biactive and switcher nodes) exhibited significantly higher gradient values than the shaker nodes and the stabilizer nodes (all  $p < 0.039$ , Fig. 2d). Furthermore, the transmodal nodes exhibited significantly lower T1w/T2w values than the stabilizer nodes (all  $p < 0.008$ ), and the shaker nodes exhibited significantly higher T1w/T2w values than the biactive nodes ( $p < 0.031$ , Fig. 2e). Moreover, by matching the distribution of dynamic nodes and the cognitive term maps available from NeuroSynth, we found that shakers and stabilizers were dominantly overlapped by terms related to perception, such as “visual”, “pain” and “auditory”, while biactive and switcher nodes emphasized terms involving more abstract and complex functions, such as “memory”, “emotion” and “reward” (Fig. 2f). These findings suggest that the spatial configuration of the intrinsic chronnectome reflects a large-scale cortical functional hierarchy that couples with the primary connectivity gradient, microarchitecture as well as a cognitive spectrum from perception to abstract functions.

#### 3.2. Transcriptional profiles are associated with the intrinsic chronnectome

We observed that two significant components from PLSR explained 28% of the variance in the dynamic measurements ( $p < 0.0048$ , spin test, Fig. S2). Specifically, the first component represented an association between brain network dynamics and a transcriptional profile characterized by high expression mainly in the posterior parietal-occipital areas (Fig. 3a, left). The regional mapping of this component correlated positively with tGV but negatively with tMV. The second component represented an association between network dynamics and a transcriptional profile with high expression predominantly in the anterior prefrontal and temporal areas (Fig. 3a, right), the regional mapping of which correlated positively with both tGV and tMV. Finally, the transcriptional profile of the first component was significantly enriched in genes related to the potassium ion channel complex and activity (all  $q < 0.001$ ), and the transcriptional profile of the second component was significantly enriched with genes associated with the mitochondrial part of the cellular component (all  $q < 0.0001$ ) (Figs. 3b, S3 and 4, Table S2).

We further explored the averaged expression of two significant least squares components among four types of brain nodes (spin tests, 10,000 permutations, Fig. 3c). Specifically, for genes related to the potassium ion channel, higher expression was observed in the shaker nodes than

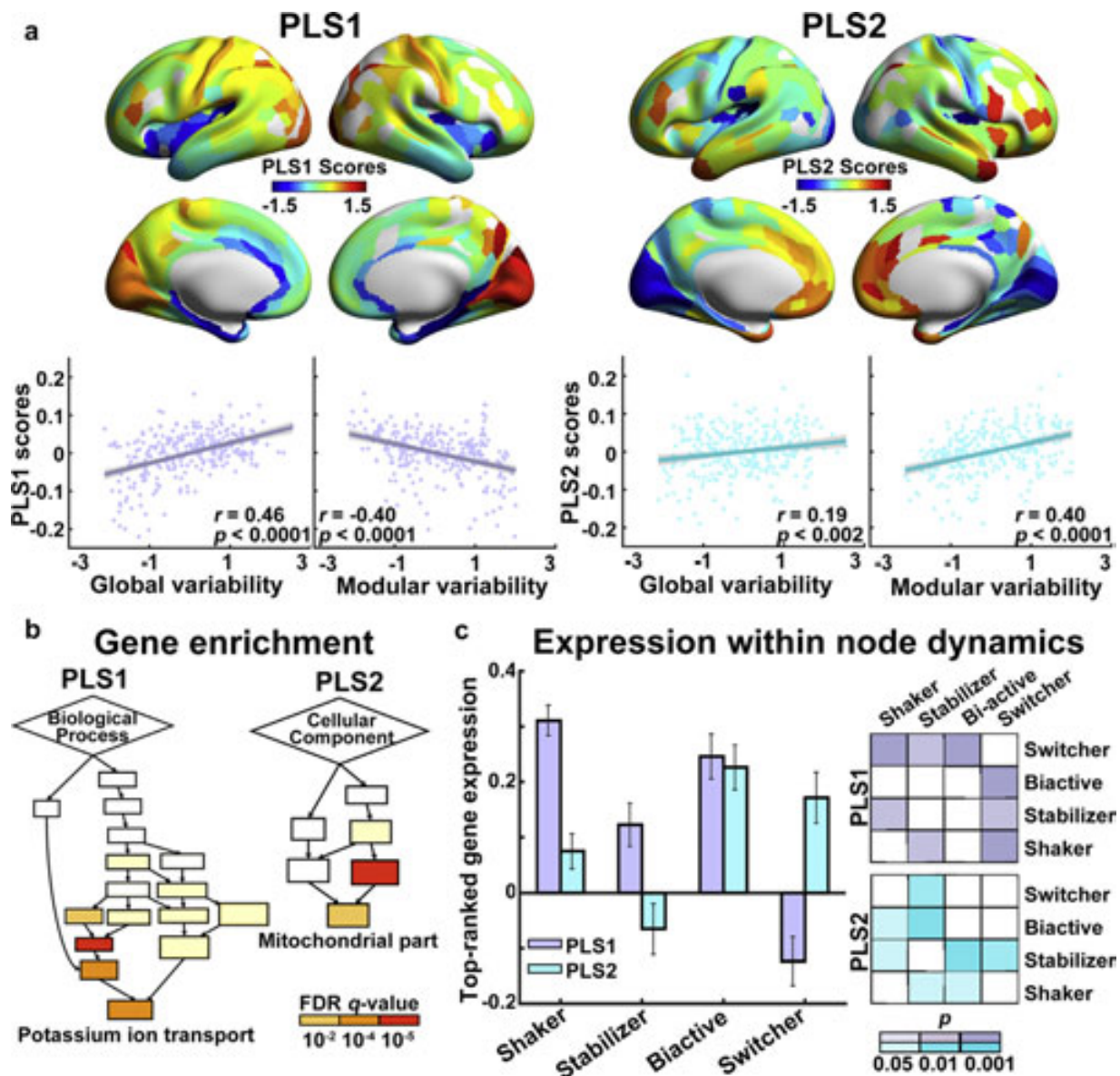


**Fig. 3.** Association between gene expression profiles and dynamic network architectures. **a**) The first two partial least squares (PLS) regression components (PLS 1 and PLS 2) explain 28% of the variance in the dynamic measures. PLS 1 identified a gene-expression profile with overexpression mainly in the medial occipital, lateral parietal, and lateral prefrontal cortices positively correlated with global dynamics but negatively correlated with modular dynamics (left column). PLS 2 identified a gene expression profile with overexpression dominantly in the medial/lateral prefrontal and lateral temporal cortices positively correlated with both global and modular dynamics (right column). The shadow indicates the 95% confidence intervals. **b**) PLS 1 is enriched for genes related to Gene Ontology of biological processes and cellular components associated with the complex and activity of potassium ion channels, whereas PLS 2 is enriched for genes related to mitochondria (colors index the  $q$ -values for significant enrichment). See Figs. S3 and 4 for more details about these Gene Ontology terms. **c**) The mean expression levels of the top 10% of weighted genes in PLS 1 and PLS 2 are diversely distributed across the four types of dynamic network nodes (left). The error bar indicates the standard error. There are significant between-group differences in the gene expression levels across the four types of nodes (right, colors index the  $p$ -values for significant between-group differences).

in the switcher and stabilizer nodes (both  $p < 0.007$ ) and in the biactive nodes than in the switcher ( $p < 0.0001$ ). For genes associated with mitochondria, higher expression was observed in the biactive nodes than in the shaker and stabilizer nodes (both  $p < 0.047$ ) and in the switcher and shaker nodes than in the stabilizer nodes (both  $p < 0.027$ ). These findings indicate the transcriptional profiles related to the different temporal dynamics of brain nodes in the chronnectome.

### 3.3. Validation results

(i) *Effect of head motion.* By analyzing the data with spike regression-based scrubbing in the nuisance regression procedure, we found that

the spatial patterns of time-varying measurements were highly similar to our main results (tGV and tMV, both  $r > 0.99$ ,  $p < 0.0001$ ; node classification, NMI = 0.93, Fig. S5a). Specifically, the spatial pattern still aligned to the cortical functional hierarchy (Fig. S5b, left), coupled well with the cortical microarchitecture (Fig. S5b, right) and was associated with gene expression profiles that were similar to the main results (Table S4 and Fig. S5c). (ii) *Effect of the dynamic network construction approach.* The spatial dynamic patterns obtained by DCC were moderately similar to our main results (tGV and tMV: both  $r = 0.83$ ,  $p < 0.0001$ ; node classification, NMI = 0.42, Fig. S6a). The distribution of the four dynamic nodes mainly followed a cortical hierarchy (Fig. S6b, left) and was relatively consistent with the main results of the microarchitecture (Fig. S6b,

right) and gene expression profiles (Table S5 and Fig. S6c). (iii) *Effect of the individual differences in dynamic measures.* Consistent with our main findings, the spatial pattern of dynamic nodes (Fig. S7a) coupled well with the cortical functional hierarchy and the cortical microarchitecture (Fig. S7b), and associated with the similar gene expression profiles (Table S6 and Fig. S7c). (iv) *Effect of the negative connectivity and network threshold in tMV calculation.* The spatial pattern of tMV without thresholding was significantly similar to our main results ( $r = 0.59, p < 0.0001$ ; node classification, NMI = 0.55, Fig. S8a). The dynamic node distribution matched a cortical hierarchy (Fig. S8b, left) but did not show the differences in microarchitecture among the four types (Fig. S8c, right). The transcriptional profiles of the first PLSR component kept consistent to the main findings while the second component was not significant in this case (Table S7 and Fig. S8c). These results suggested that the inclusion of weak and negative connections in tMV calculation may affect the spatial distribution of chronnectome and reduce the diversity among different node types. (v) *Reproducibility of the half-split analysis.* The main results were reproducible in the internal replication analysis (Table S3).

## 4. Discussion

In this study, we demonstrate the spatial heterogeneity of brain network dynamics in terms of temporal variations in global and modular organization. This architecture reflects hierarchical function processing and is coupled with the underlying microarchitecture. Importantly, the network dynamics are closely linked with the transcriptional profiles, with brain nodes having diverse expression of genes regulating the potassium ion channel activity and mitochondria. Collectively, these findings provide empirical evidence for the hierarchically organized architecture of the chronnectome and its potentially relevant neurobiological functions, which have implications for the understanding and interpretation of the organizational principle and working mechanism of brain network dynamics.

### 4.1. The intrinsic chronnectome architectures follows cortical hierarchical organization

We characterized the chronnectome architectures in terms of four categories of dynamic brain nodes (i.e., biactive, switcher, shaker, and stabilizer nodes). The spatial distributions of these nodes with distinct time-varying features are highly comparable with the cortical functional hierarchy for information processing from sensation to cognition proposed by Mesulam (1998), the principle gradient of functional connectivity reported by Margulies et al. (2016), and the underlying myeloarchitectural/microstructural features of the human brain (Glasser and Van Essen, 2011). Specifically, shaker nodes with high global fluctuations are mainly located in the primary sensory cortices, which provide obligatory portals for accessing sensory stimuli, and the primary motor cortices, which provide gateways that rely on complex responses to interact with the external world. That is, the function of primary areas addresses the most primary but continuous processing for particularly specialized sensory information (Grill-Spector and Malach, 2004). Such processing might require dramatically dynamic connectivity fluctuations for the constant monitoring and capture of information from the ever-changing external environment. The stabilizers are predominantly located in the unimodal association areas that encode the basic features of sensation captured from particular sensory modalities, such as color, motion, and sound from the primary cortex, into complex sensory experience, such as depicting objects, faces, and spatial locations (Mesulam, 1998). Given the nature of highly specialized modalities, these unimodal association areas with limited global fluctuations and intermodular switching fit this unique role in information processing. Interestingly, these two types of dynamic nodes showed high T1w/T2w

values, which may be associated with the features of heavily myelinated, dense and well-organized neurons with small dendritic arbors and earlier myelinated neurons during the development of these areas (Fuster, 1997). Thus, the relatively simple myeloarchitectural and microarchitectural features of the shaker nodes and the stabilizer nodes are in line with their functional roles in processing unimodal content reflected by less modular switching.

Importantly, the biactive nodes with both high global and modular dynamics are mainly distributed in heteromodal association regions (i.e., the lateral and medial frontal and parietal cortices). These regions play central roles in forming distributed but integrated multimodal representations and are associated with high areal expansion during development and evolution (Hill et al., 2010). The participation of the heteromodal association areas in receiving convergent inputs from multiple unimodal areas and binding with other transmodal areas usually requires global communications across distributed regions and integration among functional systems (Cole et al., 2013; Liu et al., 2017). Thus, the prodigious global connectivity fluctuations and frequent modular switching might provide a neurobiological foundation that enables the biactive nodes to meet the high requirement of complex processes in high-order cognition in the human brain. The switcher nodes with only high modular reorganization are predominantly located in the limbic and paralimbic areas. These regions are related to the internal milieu and are responsible for the regulation of emotion and motivation. The literature suggests that the limbic and paralimbic areas make up a complex organization that responds to interconnections between primitive subcortical and evolved cortical structures (Mesulam, 2000). Both biactive and switcher nodes belong to the transmodal cortices, which are the lightly myelinated areas with low neuron density but complex dendritic arbors (Elston et al., 2001) and areas with great involvement in various advanced cognitive functions (Braun et al., 2015; Gonzalez-Castillo et al., 2015; Liao et al., 2017; Liu et al., 2018; Vidaurre et al., 2017). Consistent with the findings of correlation between cognitive flexibility and temporal modular variability in our previous study (Liao et al., 2017), we also found that nodes with relatively high temporal modular switching were mainly overlapped with cognitive term maps involving more abstract functions in this study (Fig. 2f). Therefore, the high temporal variations in modular structure in the biactive and switcher nodes might provide a network foundation for the dynamic combination and integration of multimodal information across the brain to extend the flexibility for translating sensation into cognition, thereby facilitating advanced human mental and behavioral functions.

A recent study revealed a repeatable resting-state network partition based on the same Glasser-360 cortical parcellation used in the current study (Ji et al., 2019). It was observed that resting-state networks related to primary functions (e.g., visual, somatomotor, and auditory) are dominantly enriched in a single type of shaker node or stabilizer node, whereas networks with high-order cognitive functions (e.g., default mode, frontoparietal, and cingulo-opercular networks) heterogeneously comprise different types of dynamic nodes, including biactive and switcher nodes. Together, the observed dynamic architecture reflects the cognitive spectrum and cortical hierarchy of large-scale functional networks in the human brain.

### 4.2. The expression of ion channel and mitochondria-related genes is associated with the intrinsic chronnectome

We found that the gene expression profiles that can explain the spatial heterogeneity in the dynamic characteristics of the chronnectome are mainly related to ion channels and mitochondria. Ion channels are crucial structures for the generation and conduction of electrical signaling in neurons, as they allow the movement of ions across the membrane, leading to changes in membrane potential and propa-

gation of neuronal electrical signals. The summed electric current flowing from multiple nearby neurons can generate local field potentials in the extracellular space around neurons, and the dynamic fluctuations of local field potentials are associated with the hemodynamics that can be captured by fMRI (Scholvinck et al., 2010). Thus, the dynamics of macroscale brain networks are reasonably associated with the neuronal electrical activity induced by ion channels. Here, the first component represented an association between brain network dynamics and a transcriptional profile characterized by high expression mainly in the posterior parietal-occipital areas, especially the sensorimotor cortex, where shaker nodes with frequently global variability were located. Previous studies have found that the voltage-gated potassium channels contributed to high temporal precision of auditory neurons (Oak and Yi, 2014) and enabled repetitive firing at high frequencies (Rudy and McBain, 2001). This nature of voltage-gated potassium channels might facilitate the frequent global connectivity fluctuation of the shaker nodes. Our results provide implications for the potential cellular and molecular functions of the macroscale chronnectome in the resting human brain. Previous studies reported that the static functional connectivity was associated with the transcriptional profiles enriched in ion channel (Krienen et al., 2016; Richiardi et al., 2015). However, our explorational mediation analysis showed that the associations between expression of ion channel-related genes and functional dynamics were not mediated by the static functional connectivity (Fig. S9, top). Besides the static resting-state functional networks, several transcriptome-neuroimaging association studies have demonstrated that the expression of ion channel-related genes is closely related to dynamic streams in functional networks during tasks (Diez and Sepulcre, 2018) and structural networks (Romero-Garcia et al., 2018; Seidlitz et al., 2018; Whitaker et al., 2016). Therefore, we speculate that the gene expression related to ion channels might be a trans-modality (structural and functional), trans-state (rest and task), and trans-timescale (static and dynamic) molecular signature for human brain networks. More researches are needed to further clarify their complex relationship in the future.

The mitochondrion is the “powerhouse” organelle of the neuron and synthesizes adenosine triphosphate via the citric acid cycle and oxidative phosphorylation to provide energy for neuronal signaling and maintenance of the resting membrane potential (Harris et al., 2012). Our study revealed a significant coupling between the expression pattern of mitochondria-related genes and the intrinsic chronnectome pattern, with high expression dominantly found in biactive nodes (medial/lateral prefrontal and parietal cortices), which exhibit a high level of dynamic features. Consistently, the occupancy rate in the dynamic connectivity state linking most of these regions is related to a single nucleotide polymorphism component with the genes associated with metabolism (Rashid et al., 2019). These regions exhibit high levels of energy metabolism, such as glucose utilization, oxygen consumption and regional cerebral blood flow (Liang et al., 2013; Tomasi et al., 2013). A recent study focusing on brain structure demonstrated that the variation in regional scaling to the normative brain size and shape in frontoparietal regions is associated with the expression of mitochondria-related genes (Reardon et al., 2018). Moreover, these regions are essential for mediating various complex cognitive functions (Goldman-Rakic, 1988) and are phylogenetically late developing, with a disproportionate enlargement during evolution (Van Essen and Dierker, 2007). Together with the results in this study, we speculate that the large expansion and complexity in structures and functional dynamics might be supported by substitutional energy production at the cellular level. Notably, the observed transcriptional profiles were not exclusively related to dynamic network organization or any other large-scale brain networks. Our explorational mediation analysis showed that the association between expression of mitochondria-related genes and functional dynamics was partially mediated by the static functional connectivity (Fig. S9, bottom), although the causal relationship between static and dynamic connectivity remains unclear. Additional studies exploring the relation-

ship of gene expression pattern among different modalities, states, and timescales are needed in the future.

#### 4.3. Further considerations

First, the gene expression data from the AIBS were sampled from six donors with six left hemispheres and two right hemispheres. The limited sampling might have created a bias in capturing the variance in gene expression across individuals. Future studies with larger sample whole-brain genome-wide gene expression data could better address this issue. Second, a recent study showed that the hierarchy extending from the primary sensorimotor cortex to association areas in the cerebral cortex was tightly linked to a large-scale gradient in gene expression, coupled with multimodal features including the cytoarchitecture, interneuron cell densities and long-range axonal connectivity in mice (Fulcher et al., 2019). Intriguingly, they also found a significant mouse-human consistency in the hierarchical gradient. However, whether and how these underlying anatomical properties together shape the spatial layout of the human chronnectome is an important issue to be clarified. Third, in the current study, we explored the relationship between dynamic network architecture and cortical functional hierarchy focusing on the cortex. Recently, subcortical areas were also highlighted to play an indispensable role in dynamic transitions (Shine et al., 2019). The dynamic roles of subcortical areas in brain functional hierarchy is an important topic worth clarifying in the future. Fourth, we constructed the human chronnectome from multiband fMRI data. Although BOLD imaging captures hemodynamic signals that can indirectly reflect neural electrical activity (Chang et al., 2013; Logothetis et al., 2001), future studies that simultaneously collect fMRI and electrophysiological data would provide better insight into these gene-brain interactions. Fifth, several previous studies defined connector, provincial, satellite and peripheral nodes based on the stationary functional brain network (He et al., 2009; Power et al., 2013). Intuitively, there are some similarities between the spatial distribution of these stationary node types and the four types of dynamic nodes defined in this study. For example, provincial and peripheral nodes are mainly found in the primary cortex, similar to shaker nodes, and the connectors are primarily distributed in the dorsolateral prefrontal and parietal cortices, similar to biactive nodes. However, there are several differences in the spatial layout between dynamic and stationary nodes, such as switcher nodes, which are predominately located in limbic and paralimbic areas and did not match any particular stationary node. Comprehensively comparing dynamic nodes and stationary nodes in the future may improve our understanding of the regional organization in the human brain network. Sixth, here we employed a commonly used sliding window approach to construct the dynamic networks and a DCC method (Lindquist et al., 2014) as a validation analysis. Recently, novel approaches such as Hidden Markov Model have been proposed to discover a set of hidden brain states in brain functional data. Different approaches capture the dynamics of functional networks from different perspectives and there is still no gold standard for selecting the best among these dynamic approaches. Further studies are needed to investigate the abilities of different approaches in characterizing different dynamic features of functional brain network and to develop better approaches to minimize noise and evaluate the optimal parameters in dynamic network estimations and analyses. Finally, the findings reported here were correlational, not causative. Determining whether and how the genes and the brain interact remains an interesting area for further investigation.

#### Credit author statement

Yong He, Jin Liu and Mingrui Xia conceived the study; Jin Liu and Mingrui Xia performed the data analysis with technical support from Xindi Wang and Xuhong Liao; Jin Liu, Mingrui Xia and Yong He wrote the manuscript; all authors commented on the study and manuscript.

## Acknowledgments

The authors would like to thank Dr. Yanchao Bi and Dr. Tengda Zhao for helpful discussions. This work was supported by the National Key R&D Program of China (2018YFA0701402) and National Natural Science Foundation of China (81620108016, 31830034, 81671767, 81971690), the Changjiang Scholar Professorship Award (T2015027), and the Beijing Nova Program (Z191100001119023). Imaging data were provided by the Human Connectome Project, WU-Minn Consortium (Principal Investigators: David Van Essen and Kamil Ugurbil; 1U54MH091657) funded by the 16 NIH Institutes and Centers which support the NIH Blueprint for Neuroscience Research; and by the McDonnell Center for Systems Neuroscience at Washington University. The authors thank the Allen Institute for Brain Science for providing the gene expression data.

## Supplementary materials

Supplementary materials associated with this article can be found, in the online version, at doi:10.1016/j.neuroimage.2020.117296.

## References

- Alexander-Bloch, A.F., Shou, H., Liu, S., Satterthwaite, T.D., Glahn, D.C., Shinohara, R.T., Vandekar, S.N., Raznahan, A., 2018. On testing for spatial correspondence between maps of human brain structure and function. *NeuroImage* 178, 540–551.
- Allen, E.A., Damaraju, E., Plis, S.M., Erhardt, E.B., Eichele, T., Calhoun, V.D., 2014. Tracking whole-brain connectivity dynamics in the resting state. *Cereb. Cortex* 24, 663–676.
- Arloth, J., Bader, D.M., Roh, S., Altmann, A., 2015. Re-annotator: annotation pipeline for microarray probe sequences. *PLoS One* 10, e0139516.
- Arnatkeviciute, A., Fulcher, B.D., Fornito, A., 2019. A practical guide to linking brain-wide gene expression and neuroimaging data. *NeuroImage* 189, 353–367.
- Bassett, D.S., Wymbs, N.F., Porter, M.A., Mucha, P.J., Carlson, J.M., Graston, S.T., 2011. Dynamic reconfiguration of human brain networks during learning. *Proc. Natl. Acad. Sci. U.S.A.* 108, 7641–7646.
- Biswal, B., Yetkin, F.Z., Haughton, V.M., Hyde, J.S., 1995. Functional connectivity in the motor cortex of resting human brain using echo-planar MRI. *Magn. Reson. Med.* 34, 537–541.
- Braun, U., Schafer, A., Walter, H., Erk, S., Romanczuk-Seiferth, N., Haddad, L., Schweiger, J.I., Grimm, O., Heinz, A., Tost, H., Meyer-Lindenberg, A., Bassett, D.S., 2015. Dynamic reconfiguration of frontal brain networks during executive cognition in humans. *Proc. Natl. Acad. Sci. U.S.A.* 112, 11678–11683.
- Burt, J.B., Demirtas, M., Eckner, W.J., Navejar, N.M., Ji, J.L., Martin, W.J., Bernacchia, A., Anticevic, A., Murray, J.D., 2018. Hierarchy of transcriptomic specialization across human cortex captured by structural neuroimaging topography. *Nat. Neurosci.* 21, 1251–1259.
- Calhoun, V.D., Miller, R., Pearson, G., Adali, T., 2014. The chronnectome: time-varying connectivity networks as the next frontier in fMRI data discovery. *Neuron* 84, 262–274.
- Chang, C., Liu, Z., Chen, M.C., Liu, X., Duyn, J.H., 2013. EEG correlates of time-varying BOLD functional connectivity. *NeuroImage* 72, 227–236.
- Choe, A.S., Nebel, M.B., Barber, A.D., Cohen, J.R., Xu, Y., Pekar, J.J., Caffo, B., Lindquist, M.A., 2017. Comparing test-retest reliability of dynamic functional connectivity methods. *NeuroImage* 158, 155–175.
- Cole, M.W., Reynolds, J.R., Power, J.D., Repovs, G., Anticevic, A., Braver, T.S., 2013. Multi-task connectivity reveals flexible hubs for adaptive task control. *Nat. Neurosci.* 16, 1348–1355.
- Deco, G., Jirsa, V.K., McIntosh, A.R., 2013. Resting brains never rest: computational insights into potential cognitive architectures. *Trends Neurosci.* 36, 268–274.
- Diez, I., Sepulcre, J., 2018. Neurogenetic profiles delineate large-scale connectivity dynamics of the human brain. *Nat. Commun.* 9, 3876.
- Eden, E., Navon, R., Steinfeld, I., Lipson, D., Yakhini, Z., 2009. GOrilla: a tool for discovery and visualization of enriched GO terms in ranked gene lists. *BMC Bioinform.* 10, 48.
- Elston, G.N., Benavides-Piccione, R., DeFelipe, J., 2001. The pyramidal cell in cognition: a comparative study in human and monkey. *J. Neurosci.* 21, RC163.
- Elton, A., Gao, W., 2015. Task-related modulation of functional connectivity variability and its behavioral correlations. *Hum. Brain Mapp.* 36, 3260–3272.
- Ffytche, D.H., Wible, C.G., 2014. From tones in tinnitus to sensed social interaction in schizophrenia: how understanding cortical organization can inform the study of hallucinations and psychosis. *Schizophr. Bull.* 40 (Suppl 4) S305–316.
- Fong, A.H.C., Yoo, K., Rosenberg, M.D., Zhang, S., Li, C.R., Scheinost, D., Constable, R.T., Chun, M.M., 2019. Dynamic functional connectivity during task performance and rest predicts individual differences in attention across studies. *NeuroImage* 188, 14–25.
- Fornito, A., Arnatkeviciute, A., Fulcher, B.D., 2019. Bridging the gap between connectome and transcriptome. *Trends Cogn. Sci.* 23, 34–50.
- Fulcher, B.D., Murray, J.D., Zerbi, V., Wang, X.J., 2019. Multimodal gradients across mouse cortex. *Proc. Natl. Acad. Sci. U.S.A.* 116, 4689–4695.
- Fuster, J.M., 1997. Network memory. *Trends Neurosci.* 20, 451–459.
- Glasser, M.F., Coalson, T.S., Robinson, E.C., Hacker, C.D., Harwell, J., Yacoub, E., Ugurbil, K., Andersson, J., Beckmann, C.F., Jenkinson, M., Smith, S.M., Van Essen, D.C., 2016. A multi-modal parcellation of human cerebral cortex. *Nature* 536, 171–178.
- Glasser, M.F., Sotiropoulos, S.N., Wilson, J.A., Coalson, T.S., Fischl, B., Andersson, J.L., Xu, J., Jbabdi, S., Webster, M., Polimeni, J.R., Van Essen, D.C., Jenkinson, M., Consortium, W.U.-M.H., 2013. The minimal preprocessing pipelines for the Human Connectome Project. *NeuroImage* 80, 105–124.
- Glasser, M.F., Van Essen, D.C., 2011. Mapping human cortical areas in vivo based on myelin content as revealed by T1- and T2-weighted MRI. *J. Neurosci.* 31, 11597–11616.
- Goldman-Rakic, P.S., 1988. Topography of cognition: parallel distributed networks in primate association cortex. *Annu. Rev. Neurosci.* 11, 137–156.
- Gonzalez-Castillo, J., Hoy, C.W., Handwerker, D.A., Robinson, M.E., Buchanan, L.C., Saad, Z.S., Bandettini, P.A., 2015. Tracking ongoing cognition in individuals using brief, whole-brain functional connectivity patterns. *Proc. Natl. Acad. Sci. U.S.A.* 112, 8762–8767.
- Grill-Spector, K., Malach, R., 2004. The human visual cortex. *Annu. Rev. Neurosci.* 27, 649–677.
- Harris, J.J., Jolivet, R., Attwell, D., 2012. Synaptic energy use and supply. *Neuron* 75, 762–777.
- Hawrylycz, M.J., Levin, E.S., Guillozet-Bongaarts, A.L., Shen, E.H., Ng, L., Miller, J.A., van de Lagemaat, L.N., Smith, K.A., Ebbert, A., Riley, Z.L., Abajian, C., Beckmann, C.F., Bernard, A., Bertagnolli, D., Boe, A.F., Cartagena, P.M., Chakravarty, M.M., Chapin, M., Chong, J., Dalley, R.A., David Daly, B., Dang, C., Datta, S., Dee, N., Dolbeare, T.A., Faber, V., Feng, D., Fowler, D.R., Goldy, J., Gregor, B.W., Haradon, Z., Haynor, D.R., Hohmann, J.G., Horvath, S., Howard, R.E., Jeromin, A., Jochim, J.M., Kinnunen, M., Lau, C., Lazarz, E.T., Lee, C., Lemon, T.A., Li, L., Li, Y., Morris, J.A., Overly, C.C., Parker, P.D., Parry, S.E., Reding, M., Royall, J.J., Schulkin, J., Sequeira, P.A., Slaughterbeck, C.R., Smith, S.C., Sodt, A.J., Sunkin, S.M., Swanson, B.E., Vawter, M.P., Williams, D., Wahnoutka, P., Zielke, H.R., Geschwind, D.H., Hof, P.R., Smith, S.M., Koch, C., Grant, S.G.N., Jones, A.R., 2012. An anatomically comprehensive atlas of the adult human brain transcriptome. *Nature* 489, 391–399.
- He, Y., Wang, J., Wang, L., Chen, Z.J., Yan, C., Yang, H., Tang, H., Zhu, C., Gong, Q., Zang, Y., Evans, A.C., 2009. Uncovering intrinsic modular organization of spontaneous brain activity in humans. *PLoS One* 4, e5226.
- Hill, J., Inder, T., Neil, J., Dierker, D., Harwell, J., Van Essen, D., 2010. Similar patterns of cortical expansion during human development and evolution. *Proc. Natl. Acad. Sci. U.S.A.* 107, 13135–13140.
- Huntenburg, J.M., Bazin, P.L., Margulies, D.S., 2018. Large-scale gradients in human cortical organization. *Trends Cogn. Sci.* 22, 21–31.
- Hutchison, R.M., Womelsdorf, T., Allen, E.A., Bandettini, P.A., Calhoun, V.D., Corbetta, M., Della Penna, S., Duyn, J.H., Glover, G.H., Gonzalez-Castillo, J., Handwerker, D.A., Keilholz, S., Kiviniemi, V., Leopold, D.A., de Pasquale, F., Sporns, O., Walter, M., Chang, C., 2013. Dynamic functional connectivity: promise, issues, and interpretations. *NeuroImage* 80, 360–378.
- Ji, J.L., Spronk, M., Kulkarni, K., Repovs, G., Anticevic, A., Cole, M.W., 2019. Mapping the human brain's cortical-subcortical functional network organization. *NeuroImage* 185, 35–57.
- Kang, J., Wang, L., Yan, C., Wang, J., Liang, X., He, Y., 2011. Characterizing dynamic functional connectivity in the resting brain using variable parameter regression and Kalman filtering approaches. *NeuroImage* 56, 1222–1234.
- Kent, W.J., Sugnet, C.W., Furey, T.S., Roskin, K.M., Pringle, T.H., Zahler, A.M., Hausler, D., 2002. The human genome browser at UCSC. *Genome Res.* 12, 996–1006.
- Kiehl, K.A., 2006. A cognitive neuroscience perspective on psychopathy: evidence for parabolic system dysfunction. *Psychiatry Res.* 142, 107–128.
- Krienen, F.M., Yeo, B.T., Ge, T., Buckner, R.L., Sherwood, C.C., 2016. Transcriptional profiles of supragranular-enriched genes associate with corticocortical network architecture in the human brain. *Proc. Natl. Acad. Sci. U.S.A.* 113, E469–E478.
- Kruschwitz, J.D., Meyer-Lindenberg, A., Veer, I.M., Wackerhagen, C., Erk, S., Mohnke, S., Pohland, L., Haddad, L., Grimm, O., Tost, H., Romanczuk-Seiferth, N., Heinz, A., Walter, M., Walter, H., 2015. Segregation of face sensitive areas within the fusiform gyrus using global signal regression? A study on amygdala resting-state functional connectivity. *Hum. Brain Mapp.* 36, 4089–4103.
- Liang, X., Zou, Q., He, Y., Yang, Y., 2013. Coupling of functional connectivity and regional cerebral blood flow reveals a physiological basis for network hubs of the human brain. *Proc. Natl. Acad. Sci. U.S.A.* 110, 1929–1934.
- Liao, X., Cao, M., Xia, M., He, Y., 2017. Individual differences and time-varying features of modular brain architecture. *NeuroImage* 152, 94–107.
- Liao, X., Yuan, L., Zhao, T., Dai, Z., Shu, N., Xia, M., Yang, Y., Evans, A., He, Y., 2015. Spontaneous functional network dynamics and associated structural substrates in the human brain. *Front. Hum. Neurosci.* 9, 478.
- Lindquist, M.A., Xu, Y., Nebel, M.B., Caffo, B.S., 2014. Evaluating dynamic bivariate correlations in resting-state fMRI: a comparison study and a new approach. *NeuroImage* 101, 531–546.
- Liu, J., Liao, X., Xia, M., He, Y., 2018. Chronnectome fingerprinting: Identifying individuals and predicting higher cognitive functions using dynamic brain connectivity patterns. *Hum. Brain Mapp.* 39, 902–915.
- Liu, J., Xia, M., Dai, Z., Wang, X., Liao, X., Bi, Y., He, Y., 2017. Intrinsic brain hub connectivity underlies individual differences in spatial working memory. *Cereb. Cortex* 27, 5496–5508.
- Logothetis, N.K., Pauls, J., Augath, M., Trinath, T., Oeltermann, A., 2001. Neurophysiological investigation of the basis of the fMRI signal. *Nature* 412, 150–157.
- Margulies, D.S., Ghosh, S.S., Goulas, A., Falkiewicz, M., Huntenburg, J.M., Langs, G., Bezgin, G., Eickhoff, S.B., Castellanos, F.X., Petrides, M., Jefferies, E., Smallwood, J., 2016. Situating the default-mode network along a principal gradient of macroscale cortical organization. *Proc. Natl. Acad. Sci. U.S.A.* 113, 12574–12579.

- Mesulam, M.M., 1998. From sensation to cognition. *Brain* 121 (Pt 6), 1013–1052.
- Mesulam, M.M., 2000. *Principles of Behavioral and Cognitive Neurology*. Oxford University Press.
- Oak, M.H., Yi, E., 2014. Voltage-gated K(+) channels contributing to temporal precision at the inner hair cell-auditory afferent nerve fiber synapses in the mammalian cochlea. *Arch. Pharm. Res.* 37, 821–833.
- Poldrack, R.A., Mumford, J.A., Schonberg, T., Kalar, D., Barman, B., Yarkoni, T., 2012. Discovering relations between mind, brain, and mental disorders using topic mapping. *PLoS Comput. Biol.* 8, e1002707.
- Power, J.D., Cohen, A.L., Nelson, S.M., Wig, G.S., Barnes, K.A., Church, J.A., Vogel, A.C., Laumann, T.O., Miezin, F.M., Schlaggar, B.L., Petersen, S.E., 2011. Functional network organization of the human brain. *Neuron* 72, 665–678.
- Power, J.D., Fair, D.A., Schlaggar, B.L., Petersen, S.E., 2010. The development of human functional brain networks. *Neuron* 67, 735–748.
- Power, J.D., Schlaggar, B.L., Lessov-Schlaggar, C.N., Petersen, S.E., 2013. Evidence for hubs in human functional brain networks. *Neuron* 79, 798–813.
- Power, J.D., Schlaggar, B.L., Petersen, S.E., 2015. Recent progress and outstanding issues in motion correction in resting state fMRI. *NeuroImage* 105, 536–551.
- Rashid, B., Chen, J., Rashid, I., Damaraju, E., Liu, J., Miller, R., Agcaoglu, O., van Erp, T.G.M., Lim, K.O., Turner, J.A., Mathalon, D.H., Ford, J.M., Voyvodic, J., Mueller, B.A., Belger, A., McEwen, S., Potkin, S.G., Preda, A., Bustillo, J.R., Pearson, G.D., Calhoun, V.D., 2019. A framework for linking resting-state connectome/genome features in schizophrenia: A pilot study. *NeuroImage* 184, 843–854.
- Reardon, P.K., Seidlitz, J., Vandekar, S., Liu, S., Patel, R., Park, M.T.M., Alexander-Bloch, A., Clasen, L.S., Blumenthal, J.D., Lalonde, F.M., Giedd, J.N., Gur, R.C., Gur, R.E., Lerch, J.P., Chakravarty, M.M., Satterthwaite, T.D., Shinohara, R.T., Raznahan, A., 2018. Normative brain size variation and brain shape diversity in humans. *Science* 360, 1222–1227.
- Richiardi, J., Altmann, A., Milazzo, A.C., Chang, C., Chakravarty, M.M., Banaschewski, T., Barker, G.J., Bokde, A.L., Bromberg, U., Buchel, C., Conrod, P., Fauth-Bühler, M., Flor, H., Frouin, V., Gallinat, J., Garavan, H., Gowland, P., Heinz, A., Lemaitre, H., Mann, K.F., Martinot, J.L., Nees, F., Paus, T., Pausova, Z., Rietschel, M., Robbins, T.W., Smolka, M.N., Spanagel, R., Strohle, A., Schumann, G., Hawrylycz, M., Poline, J.B., Greicius, M.D., consortium, I., 2015. BRAIN NETWORKS. Correlated gene expression supports synchronous activity in brain networks. *Science* 348, 1241–1244.
- Romero-Garcia, R., Whitaker, K.J., Vasa, F., Seidlitz, J., Shinn, M., Fonagy, P., Dolan, R.J., Jones, P.B., Goodyer, I.M., Consortium, N., Bullmore, E.T., Vertes, P.E., 2018. Structural covariance networks are coupled to expression of genes enriched in supragranular layers of the human cortex. *NeuroImage* 171, 256–267.
- Rosvall, M., Bergstrom, C.T., 2008. Maps of random walks on complex networks reveal community structure. *Proc. Natl. Acad. Sci. U.S.A.* 105, 1118–1123.
- Rubinov, M., Sporns, O., 2010. Complex network measures of brain connectivity: uses and interpretations. *NeuroImage* 52, 1059–1069.
- Rudy, B., McBain, C.J., 2001. Kv3 channels: voltage-gated K+ channels designed for high-frequency repetitive firing. *Trends Neurosci.* 24, 517–526.
- Scholvinck, M.L., Maier, A., Ye, F.Q., Duyn, J.H., Leopold, D.A., 2010. Neural basis of global resting-state fMRI activity. *Proc. Natl. Acad. Sci. U.S.A.* 107, 10238–10243.
- Seidlitz, J., Vasa, F., Shinn, M., Romero-Garcia, R., Whitaker, K.J., Vertes, P.E., Wagstyl, K., Kirkpatrick Reardon, P., Clasen, L., Liu, S., Messenger, A., Leopold, D.A., Fonagy, P., Dolan, R.J., Jones, P.B., Goodyer, I.M., Consortium, N., Raznahan, A., Bullmore, E.T., 2018. Morphometric similarity networks detect microscale cortical organization and predict inter-individual cognitive variation. *Neuron* 97, 231–247 e237.
- Shine, J.M., Breakspear, M., Bell, P.T., Ehgoetz Martens, K.A., Shine, R., Koyejo, O., Sporns, O., Poldrack, R.A., 2019. Human cognition involves the dynamic integration of neural activity and neuromodulatory systems. *Nat. Neurosci.* 22, 289–296.
- Shine, J.M., Koyejo, O., Poldrack, R.A., 2016. Temporal metastates are associated with differential patterns of time-resolved connectivity, network topology, and attention. *Proc. Natl. Acad. Sci. U.S.A.* 113, 9888–9891.
- Steen, M., Hayasaka, S., Joyce, K., Laurienti, P., 2011. Assessing the consistency of community structure in complex networks. *Phys. Rev. E Stat. Nonlinear Soft Matter Phys.* 84, 016111.
- Telesford, Q.K., Lynall, M.E., Vettel, J., Miller, M.B., Grafton, S.T., Bassett, D.S., 2016. Detection of functional brain network reconfiguration during task-driven cognitive states. *NeuroImage* 142, 198–210.
- Tomasi, D., Wang, G.J., Volkow, N.D., 2013. Energetic cost of brain functional connectivity. *Proc. Natl. Acad. Sci. U.S.A.* 110, 13642–13647.
- Van Essen, D.C., Dierker, D.L., 2007. Surface-based and probabilistic atlases of primate cerebral cortex. *Neuron* 56, 209–225.
- Van Essen, D.C., Smith, S.M., Barch, D.M., Behrens, T.E., Yacoub, E., Ugurbil, K., Consortium, W.U.-M.H., 2013. The WU-Minn Human Connectome Project: an overview. *NeuroImage* 80, 62–79.
- Vertes, P.E., Rittman, T., Whitaker, K.J., Romero-Garcia, R., Vasa, F., Kitzbichler, M.G., Wagstyl, K., Fonagy, P., Dolan, R.J., Jones, P.B., Goodyer, I.M., Consortium, N., Bullmore, E.T., 2016. Gene transcription profiles associated with inter-modular hubs and connection distance in human functional magnetic resonance imaging networks. *Philos. Trans. R Soc. Lond. B Biol. Sci.* 371.
- Vidaurre, D., Smith, S.M., Woolrich, M.W., 2017. Brain network dynamics are hierarchically organized in time. *Proc. Natl. Acad. Sci. U.S.A.* 114, 12827–12832.
- Vinh, N.X., Epps, J., Bailey, J., 2010. Information theoretic measures for clusterings comparison: variants, properties, normalization and correction for chance. *J. Mach. Learn. Res.* 11, 2837–2854.
- Wang, J., Wang, X., Xia, M., Liao, X., Evans, A., He, Y., 2015. GREYNET: a graph theoretical network analysis toolbox for imaging connectomics. *Front. Hum. Neurosci.* 9, 386.
- Whitaker, K.J., Vertes, P.E., Romero-Garcia, R., Vasa, F., Moutoussis, M., Prabhu, G., Weiskopf, N., Callaghan, M.F., Wagstyl, K., Rittman, T., Tait, R., Ooi, C., Suckling, J., Inkster, B., Fonagy, P., Dolan, R.J., Jones, P.B., Goodyer, I.M., Consortium, N., Bullmore, E.T., 2016. Adolescence is associated with genomically patterned consolidation of the hubs of the human brain connectome. *Proc. Natl. Acad. Sci. U.S.A.* 113, 9105–9110.
- Xia, M., Wang, J., He, Y., 2013. BrainNet Viewer: a network visualization tool for human brain connectomics. *PLoS One* 8, e68910.
- Yan, C.G., Cheung, B., Kelly, C., Colcombe, S., Craddock, R.C., Di Martino, A., Li, Q., Zuo, X.N., Castellanos, F.X., Milham, M.P., 2013. A comprehensive assessment of regional variation in the impact of head micromovements on functional connectomics. *NeuroImage* 76, 183–201.
- Zalesky, A., Fornito, A., Cocchi, L., Gollo, L.L., Breakspear, M., 2014. Time-resolved resting-state brain networks. *Proc. Natl. Acad. Sci. U.S.A.* 111, 10341–10346.